Journal of Computational Physics 228 (2009) 1380–1390

Contents lists available at ScienceDirect

Journal of Computational Physics

journal homepage: www.elsevier.com/locate/jcp

Precursor simulations in spreading using a multi-mesh adaptive finite element method

Yana Di [a,*], Xiao-Ping Wang [b]

[a] Institute of Computational Mathe. and Sci./Eng. Computing, Academy of Mathematics and Systems Science, Chinese Academy of Sciences, Beijing, China
[b] Department of Mathematics, Hong Kong University of Science and Technology, Clear Water Bay, Kowloon, Hong Kong, China

ARTICLE INFO

Article history:
Received 30 July 2008
Received in revised form 22 September 2008
Accepted 18 October 2008
Available online 5 November 2008

Keywords:
Multi-mesh
Adaptive finite element
Wetting and spreading
Precursor film
Diffuse-interface model

ABSTRACT

Using the phase-field model for immiscible two-phase flows, we have numerically investigated the wetting dynamics. The long-range van der Waals forces towards the solid, which drive the spreading of the wetting phase into the nonwetting phase, have been explicitly taken into account in the governing equations. Our continuum model uses the generalized Navier boundary condition (GNBC) to account for the fluid slipping at the solid surface. The accurate description of the molecular-scale contact-line hydrodynamics makes the numerical simulations cost too much to abide. In this work, we propose an efficient multi-mesh adaptive finite element method which approximates different components of the solution (velocity, pressure and phase variable) on different *h*-adaptive meshes because of their strongly different local behaviors. That allows us to study the early stage of spreading, wherein the precursor is initiated and developed if the van der Waals forces are strong enough. We find that there is indeed a transition in the spreading behavior across a critical value of the Hamaker constant. In particular, this critical value is noted to be the one that separates the partial wetting from complete wetting.

1. Introduction

If a small liquid drop is deposited on a solid, three interfaces come into play, and three interfacial tensions are involved: γ_{SV}, γ_{SL}, and γ, which are solid–vapor, solid–liquid, and liquid–vapor interfacial tensions, respectively. The important quantity is the spreading coefficient $S = \gamma_{SV} - \gamma_{SL} - \gamma$. The case where $S < 0$, is referred to as partial wetting: the liquid remains as a drop on the solid and reaches an equilibrium shape. For $S > 0$, the drop spontaneously spreads and tends to cover the solid surface. Such a situation is called complete wetting. When a spreading liquid completely wets a substrate it forms a very thin film and the long-range character of the molecular interactions must be taken into account. Ahead of the macroscopic front, we have seen that van der Waals (VW) forces lead to the formation of a mesoscopic precursor film [4,8]. The precursor films play a crucial role in the dynamics of the wetting of a solid surface by a liquid. However, understanding the wetting dynamics involving precursor films has not been an easy task because several distinct length scales are simultaneously presented in this truly multiscale problem: (i) behind the nominal contact line there is a macroscopic wedge of liquid advancing along the solid, (ii) ahead of the wedge there is a precursor film extending over a mesoscopic distance, and (iii) the precursor film ends at a real contact line of molecular length scale. The purpose of the present work is to investigate the early stage of spreading when the precursor is initiated and developed and the dynamics in the (molecular-scale) vicinity of the real contact line needs to be explicitly taken into account.

* Corresponding author. Tel.: +86 10 62587584; fax: +86 10 62542285.
E-mail address: yndi@lsec.cc.ac.cn (Y. Di).

0021-9991/$ - see front matter © 2008 Elsevier Inc. All rights reserved.
doi:10.1016/j.jcp.2008.10.028

Considerable work has recently been devoted to diffuse-interface models, either in the guise of the Cahn–Hilliard model for immiscible fluids [2,7,12,13,15] or the van der Waals model for a liquid–vapor interface [11]. The interface is no longer treated as a mathematical surface of zero thickness, but is rather described by the profile of an order parameter ϕ that is constant in either phase. As a result, the Navier Stokes equation acquires an extra term involving $\nabla\phi$, which models surface tension, and an additional equation for ϕ itself closes the system. In [12], a generalized Navier boundary condition (GNBC) is proposed by Qian et al. for the moving contact line problem. By combining the GNBC with the Cahn-Hilliard diffusive interface model, they have obtained numerical results that can quantitatively reproduce the molecular dynamics simulation results.

In this paper, we will use the continuum hydrodynamic model developed in [12] to investigate the development of precursor in the early stage of spreading, driven by the attractive VW forces toward the solid. In our model, we consider a two-phase immiscible fluid on a clean, flat solid surface, with one phase (the wetting phase) attracted towards the solid by the VW forces. Since the phase-field function ϕ is to provide the interface information, it is only needed to be fully resolved around the transient layers with its area much smaller than the full computational domain. The mesh adaptive method is the most natural way to improve the numerical efficiency [17]. Meanwhile, for the Navier–Stokes equation, if the liquid film thickness is in the mesoscopic range, one can still ignore the molecular nature of the liquid and consider it as continuous. The long-range molecular interactions is then described in terms of the so-called disjoining pressure [4] (here the van der Waals interactions). When the thickness of the film becomes macroscopic, the disjoining pressure vanishes. Although both phase field and velocity field undergo rapid change across the interface and around the thin liquid film, their behaviors are quite different. A multi-mesh strategy seems necessary in order to enhance the computational efficiency. In [9], a multi-mesh *h*-adaptive algorithm was proposed which approximates different variables on different meshes. Such multi-mesh adaptive finite element methods are used successfully to simulate the dendritic growth in two- and three-dimensions [6]. Here we will extend the multi-mesh technique to solve the spreading and wetting problems, where the phase-field function ϕ, the pressure p, and the velocity $\mathbf{v}$ are solved on two different adaptive meshes according to their solution behavior.

The paper is organized as follows. In Section 2, we give a brief review of the phase-field model for the contact-line motion in immiscible two-phase flows incorporating the VW forces. In Section 3, we describe the finite element discretization and the multi-mesh adaption technique. The numerical results are presented in Section 4. The paper is concluded in Section 5 with several remarks.

2. Continuum phase-field model

The diffuse-interface model has been widely used to describe the continuum hydrodynamics in immiscible two-phase flows. In particular, it has been used to remove the contact-line stress singularity. The recent discovery of the generalized Navier boundary condition (GNBC) together with the continuum model proposed in [12] have provided an accurate description for the moving contact-line hydrodynamics in immiscible two-phase flows.

2.1. Governing equations and boundary conditions

For a sharp interface impenetrable by the flow, considering the phase-field ϕ measuring the relative concentration of the two fluid phases, the pure kinematic condition can be expressed as

$$\phi_t + \mathbf{v}\cdot\nabla\phi = 0, \tag{2.1}$$

which describes the transport of the phase field by the flow. The dynamics of ϕ in a diffuse-interface description can be relaxed (or approximated) using either the relaxational Allen–Cahn equation or the diffusive Cahn–Hillard equation. In the following, we choose to use the Allen–Cahn dynamics whose numerical treatment is simpler than that of the Cahn–Hilliard equation which involves fourth-order derivatives. It is well known that, being a continuity equation, the Cahn–Hilliard equation treats the phase field as a conserved quantity, while under the Allen–Cahn equation the phase field is not conserved. Therefore, a Lagrange multiplier is introduced to the Allen–Cahn equation to enforce the conservation of ϕ [5,10]. The modified Allen–Cahn equation reads:

$$\phi_t + \mathbf{v}\cdot\nabla\phi = -M_1[\mu + \lambda(t)], \quad \frac{d}{dt}\int_\Omega \phi dx = 0, \tag{2.2}$$

where M_1 is a positive parameter responsible for the rate of relaxation, $\mu = -K\nabla^2\phi + f'(\phi)$ is the chemical potential with $f(\phi) = -\phi^2/2 + \phi^4/4$. $\lambda(t)$ is the Lagrange multiplier, which can be derived from

$$\lambda(t) = \frac{1}{|\Omega|}\left[\int_\Omega (\phi^3 - \phi)d\Omega - \int_\Gamma \partial_n\phi d\Gamma\right]. \tag{2.3}$$

The two coupled equations of motion are the convection-diffusion equation for the phase field and the Navier–Stokes equation in the presence of the capillary force density as proposed in [12]. To facilitate the numerical computation, the governing equations and boundary conditions are non-dimensionalized, with ϕ scaled by $|\phi_\pm| = \sqrt{r/u}$, lengths by $\xi = \sqrt{K/r}$, velocity by the reference speed V_0, time by ξ/V_0, pressure/stress by $\eta V_0/\xi$, and force density by $\eta V_0/\xi^2$. The Lagrange multiplier is scaled by $K|\phi_\pm|/\xi^2$. The dimensionless equations are

$$\frac{\partial \phi}{\partial t} + \mathbf{v}\cdot\nabla\phi = -\mathcal{L}_d[-\nabla^2\phi - \phi + \phi^3 + \lambda(t)], \tag{2.4}$$

$$\mathcal{R}\left[\frac{\partial \mathbf{v}}{\partial t} + (\mathbf{v}\cdot\nabla)\mathbf{v}\right] = -\nabla p + \nabla^2\mathbf{v} + \mathcal{B}(-\nabla^2\phi - \phi + \phi^3)\nabla\phi + \mathbf{f}, \tag{2.5}$$

$$\nabla\cdot\mathbf{v} = 0, \tag{2.6}$$

where $\mathbf{f} = \{f^1, f^2\}^T$ is the external force. The boundary conditions at the solid surface are the impermeability conditions $\partial_n\mu = 0, v_n = 0$, the relaxational condition for ϕ

$$\frac{\partial \phi}{\partial t} + v_\tau\partial_\tau\phi = -\mathcal{V}_s\left[\partial_n\phi - \frac{\sqrt{2}\pi}{6}\cos\theta_s\cos\left(\frac{\pi\phi}{2}\right)\right], \tag{2.7}$$

and the GNBC for v_τ

$$\frac{v_\tau^{slip}}{\mathcal{L}_s(\phi)} = -(\partial_n v_\tau + \partial_\tau v_n) + \mathcal{B}\left[\partial_n\phi - \frac{\sqrt{2}\pi}{6}\cos\theta_s\cos\left(\frac{\pi\phi}{2}\right)\right]\partial_\tau\phi. \tag{2.8}$$

The five dimensionless parameters that appear in the above equations are

- $\mathcal{L}_d = \frac{M_1\xi\Gamma}{V_0}$, which controls the rate of interfacial relaxation;
- $\mathcal{R} = \frac{\rho V_0\xi}{\eta}$; which is the Reynolds number;
- $\mathcal{B} = \frac{\Gamma^2\xi}{u\eta V_0} = \frac{3\gamma}{2\sqrt{2}\eta V_0}$, which is inversely proportional to the capillary number $\eta V_0/\gamma$;
- $\mathcal{V}_s = \frac{K\Gamma}{V_0}$; which is the relaxation parameter;
- $\mathcal{L}_s(\phi) = \frac{\eta}{\beta(\phi)\xi} = \frac{l_s(\phi)}{\xi}$, which is the slip length. Here $\beta(\phi) = \frac{1-\phi}{2}\beta_1 + \frac{1+\phi}{2}\beta_2$, with β_1 and β_2 being the slip coefficients for the ϕ_+ and ϕ_- phases, respectively.

The values of the dimensional and dimensionless parameters are given in Tables 1 and 2.

2.2. van der Waals interaction

If the spreading liquid film thickness is in the mesoscopic range, the long-range character of the molecular interactions must be taken into account. In our models, we choose the non-retarded van der Waals interactions. The potential energy density of a liquid film spreading on a solid wall varies as

$$W(y) = \frac{A}{6\pi(y+b)^3}\frac{1+\phi}{2}. \tag{2.9}$$

Here A is the so-called Hamaker constant, b is a small distance of molecular scale, and $(1+\phi)/2$ ensures the VW potential to be present in the wetting phase of $\phi = 1$ only. The energy of a film increases as the thickness decreases and the van der Waals interaction has a thickening effect. The corresponding VW force density is obtained from $dW(y)/dy$ as

$$f_{VW}(y) = -\frac{A}{2\pi(y+b)^4}\frac{1+\phi}{2}. \tag{2.10}$$

Here the fluid is in the half space of $y \geqslant 0$, and the molecular distance b arises from a void layer between the boundary of the fluid ($y = 0$) and the physical solid surface below, caused by the short-range repulsive molecular interactions between fluid and solid. A molecular length a is defined via $a^2 = A/6\pi\gamma$. The dimensionless VW force density is

Table 1
Parameter values determined from MD simulations and used in continuum models.

$\rho \approx 0.81m/\sigma^3$	$\eta \approx 1.95\sqrt{m\varepsilon}/\sigma^2$
$l_{s1} = \eta/\beta_1 \approx 1.3\sigma$	$l_{s2} = \eta/\beta_2 \approx 1.3\sigma$
$\xi \approx 0.33\sigma$	$\gamma \approx 5.5\varepsilon/\sigma^2$
$M_1 \approx 0.21\sigma^2/\sqrt{m\varepsilon}$	$\Gamma \approx 0.66\sigma/\sqrt{m\varepsilon}$
$\lvert\phi_\pm\rvert = 1$	$\cos\theta_s = 0$

Table 2
Dimensionless parameter values evaluated with $V_0 = 0.25\sqrt{\varepsilon/m}$.

$\mathcal{L}_d$	$\mathcal{R}$	$\mathcal{B}$	$\mathcal{V}_s$	$\mathcal{L}_s$
5.0	0.03	12.0	5.0	3.8

$$f_{VW}(y) = -\frac{\mathcal{A}}{2(y+b)^4}\frac{1+\phi}{2}, \tag{2.11}$$

where $\mathcal{A} = 4\sqrt{2}\mathcal{B}a^2/\xi^2$ is a dimensionless parameter.

3. The adaptive finite element solution on two meshes

In this section, we first derive the finite element approximation for our simulation model Eqs. (2.4)–(2.8). We then describe the adaptive multi-mesh technique for the Cahn-Hilliard Navier–Stokes equations.

For simplicity, we assume that Ω is a polygonal domain. Let $\mathcal{T}$ be a subdivision of Ω into simplexes (triangles or tetrahedra). As has been mentioned in the previous section, we plan to discretise the equations for ϕ and $p, \mathbf{u}$ on different meshes to explore the potential of different properties of ϕ and $p, \mathbf{u}$. Let us denote these two meshes with $\mathcal{T}_\phi$ and $\mathcal{T}_p$, respectively, which are generated from the same background triangulation $\mathcal{T}^0$ for Ω. Both triangulations will change in time adaptively with the numerical integration we use the notations $\mathcal{T}_\phi^m$ and $\mathcal{T}_p^m$ for the corresponding triangulation at time t_m. For the phase field, we define the piecewise linear finite element space $V_h^m(\mathcal{T}_\phi^m)$ with N_ϕ^m as its dimension. For the NS equation, we adopt the so-called $(P_1 iso P_2) - P_1$ elements where the pressure is piecewise linear, while the velocity has the same number of degrees of freedom as in the P_2 case but it is piecewise linear over a suitable decomposition of each triangle. If we refine $\mathcal{T}_p^m$ uniformly once and denote the refined mesh as $\mathcal{T}_u^m$, we can define piecewise linear finite element space $V_h^m(\mathcal{T}_p^m)$ with N_p^m as its dimension for the pressure and define piecewise linear finite element space $V_h^m(\mathcal{T}_u^m)$ with N_u^m as its dimension for the velocity. Then we consider the finite element approximations of unknown functions $\phi_h(\mathcal{T}_\phi^m)$ and $p_h(\mathcal{T}_p^m), \mathbf{u}_h(\mathcal{T}_u^m)$ as

$$\phi_h = \sum_{i=1}^{N_\phi} \phi_i N_i(\mathcal{T}_\phi^m), \tag{3.1}$$

and

$$\mathbf{u}_h = \sum_{i=1}^{N_u} \mathbf{u}_i N_i(\mathcal{T}_u^m), \quad p_h = \sum_{i=1}^{N_p} p_i N_i(\mathcal{T}_p^m), \tag{3.2}$$

where $\{\phi_i\}_{i=1}^{N_\phi}$, $\{p_i\}_{i=1}^{N_p}$ and $\{\mathbf{u}_i\}_{i=1}^{N_u}$ are the coefficients for phase-field variable, pressure variable and velocity variables, respectively. $\{N_i(\mathcal{T}_\phi^m)\}_{i=1}^{N_\phi}$, $\{N_i(\mathcal{T}_p^m)\}_{i=1}^{N_p}$ and $\{N_i(\mathcal{T}_u^m)\}_{i=1}^{N_u}$ are the piecewise linear finite element basis for $V_h(\mathcal{T}_\phi^m), V_h(\mathcal{T}_p^m)$ and $V_h(\mathcal{T}_u^m)$. We note that $\mathcal{T}_u^m$ is obtained from refining $\mathcal{T}_p^m$ uniformly once.

3.1. The finite element discretization

The finite element solution of the Navier–Stokes Eqs. (2.5) and (2.6) incorporating the GNBC is to find $\mathbf{u}_h \in (V_h(\mathcal{T}_u^t))^2$ and $p_h \in V_h(\mathcal{T}_p^t)$ such that

$$\begin{aligned}
&\mathcal{R}\int_\Omega \left(\frac{\partial \mathbf{u}_h}{\partial t} + \mathbf{u}_h\cdot\nabla\mathbf{u}_h\right)\cdot\mathbf{v}_h d\Omega + \int_\Omega \nabla\mathbf{u}_h\cdot\nabla\mathbf{v}_h d\Omega - \int_\Omega p_h\nabla\cdot\mathbf{v}_h d\Omega \\
&= \int_\Omega \mathbf{f}\cdot\mathbf{v}_h d\Omega + \mathcal{B}\int_\Omega \mu_h\nabla\phi_h\cdot\mathbf{v}_h d\Omega - \int_\Gamma [\mathcal{L}_s(\phi_h)]^{-1} u_{\tau,h}^{slip} v_{\tau,h} d\Gamma \\
&\quad + \mathcal{B}\int_\Gamma \left(\partial_n\phi_h - \frac{\sqrt{2}}{6}\cos\theta_s^{surf}\cos\left(\frac{\pi\phi_h}{2}\right)\partial_\tau\phi_h\right) v_{\tau,h} d\Gamma, \quad \forall \mathbf{v}_h \\
&\in (V_h(\mathcal{T}_u^t))^2,
\end{aligned} \tag{3.3}$$

$$\int_\Omega \nabla\cdot\mathbf{u}_h q_h d\Omega = 0, \quad \forall q_h \in V_h(\mathcal{T}_p^t). \tag{3.4}$$

Thanks to the fact that $\nabla^2\mathbf{u} = \nabla(\nabla\cdot\mathbf{u}) - \nabla\times\nabla\times\mathbf{u}$, we have

$$\int_\Omega \nabla p_h\cdot\nabla q_h d\Omega = -\mathcal{R}\int_\Omega (\mathbf{u}_h\cdot\nabla\mathbf{u}_h)\cdot\nabla q_h d\Omega + \int_\Omega \mathbf{f}\cdot\nabla q_h d\Omega - \int_{\partial\Omega} \mathbf{n}\times\nabla\times\mathbf{u}_h\cdot\nabla q_h + \mathcal{B}\int_\Omega \mu_h\nabla\phi_h\cdot\nabla q_h d\Omega, \tag{3.5}$$

where

$$\int_{\partial\Omega} \mathbf{n}\times\nabla\times\mathbf{u}_h\cdot\nabla q_h = \int_{\partial\Omega} ((v_x - u_y)(n_y q_x - n_x q_y) dl. \tag{3.6}$$

The weak form of the modified Allen–Cahn equation is given by

$$\int_\Omega \left(\frac{\partial \phi_h}{\partial t} + \mathbf{u}_h \cdot \nabla \phi_h\right)\psi_h d\Omega + \mathcal{L}_d \int_\Omega \nabla \phi_h \cdot \nabla \psi_h d\Omega$$
$$= \mathcal{L}_d \int_\Omega (\phi_h - \phi_h^3 - \lambda)\psi_h d\Omega + \mathcal{L}_d \int_\Gamma \left[\frac{-1}{\mathcal{V}_s}\left(\frac{\partial \phi_h}{\partial t} + \mathbf{u}_h \cdot \nabla \phi_h\right) + \frac{\sqrt{2}}{6}\cos\theta_s^{surf}\cos\left(\frac{\pi\phi_h}{2}\right)\right]\psi_h d\Gamma. \tag{3.7}$$

We introduce the following matrices and vectors:

$$K_p(i,j) = \int_\Omega \nabla N_i(\mathcal{T}_p)\cdot\nabla N_j(\mathcal{T}_p)d\Omega, \quad 1 \leqslant i,j \leqslant N_p,$$
$$F_p(\mathbf{u}_h,\phi_h)(i) = -\mathcal{R}\int_\Omega (\mathbf{u}_h\cdot\nabla\mathbf{u}_h)\cdot\nabla N_i(\mathcal{T}_p)d\Omega + \int_\Omega \mathbf{f}\cdot\nabla N_i(\mathcal{T}_p)d\Omega - \int_{\partial\Omega}\mathbf{n}\times\nabla\times\mathbf{u}_h\cdot\nabla N_i(\mathcal{T}_p)$$
$$+ \mathcal{B}\int_\Omega \mu_h\nabla\phi_h\cdot\nabla N_i(\mathcal{T}_p)d\Omega, \quad 1\leqslant i\leqslant N_p,$$
$$M_u(i,j) = \int_\Omega N_i(\mathcal{T}_u)N_j(\mathcal{T}_u)d\Omega, \quad 1\leqslant i,j\leqslant N_u,$$
$$K_u(i,j) = \int_\Omega \nabla N_i(\mathcal{T}_u)\cdot\nabla N_j(\mathcal{T}_u)d\Omega, \quad 1\leqslant i,j\leqslant N_u,$$
$$B_u(\mathbf{w}_h)(i,j) = \int_\Omega \mathbf{w}_h\cdot\nabla N_i(\mathcal{T}_u)N_j(\mathcal{T}_u)d\Omega, \quad 1\leqslant i,j\leqslant N_u,$$
$$\mathbf{D}_u(i,j) = \int_\Omega \nabla N_i(\mathcal{T}_u)N_j(\mathcal{T}_p)d\Omega, \quad 1\leqslant i\leqslant N_u, 1\leqslant j\leqslant N_p,$$
$$M_u^\Gamma(i,j) = \int_\Gamma [\mathcal{L}_s(\phi_h)]^{-1}N_i(\mathcal{T}_u)N_j(\mathcal{T}_u)d\Gamma, \quad 1\leqslant i,j\leqslant N_u,$$
$$F_u^1(\mathbf{u}_h)(i) = \int_\Omega f^1 N_i(\mathcal{T}_u)d\Omega + \mathcal{B}\int_\Omega \mu_h\frac{\partial\phi_h}{\partial x_1}N_i(\mathcal{T}_u)d\Omega + \mathcal{B}\int_\Gamma\left(\partial_n\phi_h - \frac{\sqrt{2}}{6}\cos\theta_s^{surf}\cos\left(\frac{\pi\phi_h}{2}\right)\partial_\tau\phi_h\right)N_i(\mathcal{T}_u)d\Gamma, \quad 1\leqslant i\leqslant N_u,$$
$$F_u^2(\mathbf{u}_h)(i) = \int_\Omega f^2 N_i(\mathcal{T}_u)d\Omega + \mathcal{B}\int_\Omega \mu_h\frac{\partial\phi_h}{\partial x_2}N_i(\mathcal{T}_u)d\Omega, \quad 1\leqslant i\leqslant N_u$$
$$M_\phi(i,j) = \int_\Omega N_i(\mathcal{T}_\phi)N_j(\mathcal{T}_\phi)d\Omega, \quad 1\leqslant i,j\leqslant N_\phi,$$
$$K_\phi(i,j) = \int_\Omega \nabla N_i(\mathcal{T}_\phi)\cdot\nabla N_j(\mathcal{T}_\phi)d\Omega, \quad 1\leqslant i,j\leqslant N_\phi,$$
$$B_\phi(\mathbf{w}_h)(i,j) = \int_\Omega \mathbf{w}_h\cdot\nabla N_i(\mathcal{T}_\phi)N_j(\mathcal{T}_\phi)d\Omega, \quad 1\leqslant i,j\leqslant N_\phi,$$
$$M_\phi^\Gamma(i,j) = \int_\Gamma N_i(\mathcal{T}_\phi)N_j(\mathcal{T}_\phi)d\Omega, \quad 1\leqslant i,j\leqslant N_\phi,$$
$$B_\phi^\Gamma(\mathbf{w}_h)(i,j) = \int_\Gamma \mathbf{w}_h\cdot\nabla N_i(\mathcal{T}_\phi)N_j(\mathcal{T}_\phi)d\Omega, \quad 1\leqslant i,j\leqslant N_\phi,$$
$$F_\phi(\phi_h)(i) = \mathcal{L}_d\int_\Omega(\phi_h-\phi_h^3-\lambda)N_i(\mathcal{T}_\phi)d\Omega + \mathcal{V}_s\int_\Gamma\frac{\sqrt{2}}{6}\cos\theta_s^{surf}\cos\left(\frac{\pi\phi_h}{2}\right)N_i(\mathcal{T}_\phi)d\Gamma, \quad 1\leqslant i\leqslant N_\phi.$$

Then the whole system can be written in algebraic form as

$$K_p P = F_p(\mathbf{u}_h,\phi_h), \tag{3.8a}$$
$$\mathcal{R}M_u\frac{dU^1}{dt} + M_u^\Gamma U^1 + \mathcal{R}B_u(\mathbf{u}_h)U^1 + K_u U^1 = D_u^1 P + F_u^1(\mathbf{u}_h,\phi_h), \tag{3.8b}$$
$$\mathcal{R}M_u\frac{dU^2}{dt} + \mathcal{R}B_u(\mathbf{u}_h)U^2 + K_u U^2 = D_u^2 P + F_u^2(\mathbf{u}_h,\phi_h), \tag{3.8c}$$
$$\left(M_\phi + \frac{\mathcal{L}_d}{\mathcal{V}_s}M_\phi^\Gamma\right)\frac{d\Phi}{dt} + \left(B_\phi(\mathbf{u}_h) + B_\phi^\Gamma(\mathbf{u}_h)\right)\Phi + \mathcal{L}_d K_\phi\Phi = F_\phi(\phi_h), \tag{3.8d}$$

The flow chart for the multi-mesh adaptive finite element algorithm is the following:

Prepare the background mesh $\mathcal{T}^0(\Omega)$;
Set the initial value for ϕ_h and $\mathbf{u}_h$ and $t = 0, m = 0$;
Obtain two initial meshes $\mathcal{T}_\phi^0$ and $\mathcal{T}_u^0$;
while $t < T$
do Solve the algebraic problem ((3.8)) to obtain $\mathbf{u}_h^{m+1}, p_h^{m+1}$ and ϕ_h^{m+1};
if the meshes have not been updated for N steps;

then Update mesh $\mathcal{T}_\phi$ and ϕ_h^{m+1};
Update mesh $\mathcal{T}_u$ and $\mathbf{u}_h^{m+1}$;
set $t = t + \delta t$ and $m = m + 1$;

where $\mathbf{U} = [\mathbf{u}_i], P = [p_i]$ and $\Phi = [\phi_i]$ are the unknown vectors. Here we use the semi-implicit Euler scheme for the temporal discretisation. In the above algorithm, all the algebraic linear systems are solved by algebraic multigrid method [1,3], which works quite well and often needs only 3 or 4 multigrid iterations.

3.2. The adaptive finite element solution with two meshes

The algorithm described above is implemented using C++ programming language and AFEPack, which is a common purpose adaptive finite element package with flexible data structures.

Since different meshes are used to approximate ϕ and $p, \mathbf{u}$, there exists a technical problem on how to calculate the numerical quadratures involving both meshes for ϕ and $p, \mathbf{u}$. This is rather complicated when computing the coupling terms in the system (3.8). Thanks to the hierarchical type mesh refinement algorithms for two-dimensional triangle mesh, these numerical quadratures on two meshes can be calculated efficiently because of the fact that the two meshes are based on the same background mesh and the intersection of any two different elements from different meshes is either empty or the smaller one. Thus the numerical quadratures on each element in above discretised formulas can be calculated efficiently after running over each intersection of such elements pairs [9], which can be done smoothly with the functions provided by AFEPack.

3.2.1. The mesh adaptation techniques

The main feature of our algorithm in mesh adaptation is that we use two different meshes for ϕ and $\mathbf{u}$, while the common adaptive method has only one single mesh. A reasonable error indicator is important for the mesh adaptation. Generally, *a posteriori* error estimators are used. There are many ways to derive an effective *a posteriori* estimator. One simple choice is based on the jump of gradient on the interface of two adjacent elements and the patch recovery technique [18] is the most used technique in practical computing. Plenty of excellent work have been done on this subject. More details on *a posteriori* error estimate can be found in [16]. In our computation, we adopt the L_2 norm of the jumps of finite element solution on the element boundary for both meshes. For example, if ϕ_h is the finite element solution in an element $T \in \mathcal{T}_\phi$, its heuristic error indicator can be chosen as

$$\eta_T(\phi_h) = \left(\sum_{e \in \partial T} \int_e h^3 \left[\frac{\partial \phi_h}{\partial \mathbf{n}_e} \right]^2 de \right)^{1/2},$$

where $[\cdot]$ denotes the jump on the element boundary, h is the length of edge e. In fact, the above formulation is a residual based explicit L_2 *a posteriori* estimator for elliptic operator as given in [16]. This indicator is shown to be very effective by our numerical experiments, though there is no theoretical verification for the convergence of the solutions. $\forall T \in \mathcal{T}_p$, the corresponding four elements of $\mathcal{T}_u$ are denoted as $T_i, 0 \leqslant i \leqslant 3$. Similarly, the following indicator is employed for $\mathbf{u}_h$

$$\eta_T(\mathbf{u}_h) = \left(\sum_{e \in \partial T} \int_e h^3 \left[\frac{\partial \phi_h}{\partial \mathbf{n}_e} \right]^2 de + \sum_{i=0}^{3} \sum_{e \in \partial T_i} \int_e h^3 \left[\frac{\partial \mathbf{u}_h}{\partial \mathbf{n}_e} \right] \cdot \left[\frac{\partial \mathbf{u}_h}{\partial \mathbf{n}_e} \right] de \right)^{1/2}.$$

The strategy for mesh refinement and coarsening that we adopted is the fixed threshold rule (see such as [16,14]). The fixed threshold rule, which is easy and stable in many cases, is to equi-distribute the errors on each element by ensuring the element error indicators η_T satisfying

$$\underline{\theta} \cdot tol \leqslant \eta_T \leqslant \bar{\theta} \cdot tol,$$

where tol is the prescribed tolerance and $0 < \bar{\theta}, \underline{\theta} < 1$ are two constants. As a result, it is sufficient to refine the elements where $\eta_T > \bar{\theta} tol$ and coarse the elements where $\eta_T < \underline{\theta} tol$. In practice, the tolerance is often chosen as

$$tol = \frac{\eta}{\sqrt{N}} = \left(\sum_{t \in \Delta} \eta_T^2 / N \right)^{1/2}.$$

In fact, we observe that the choice of tolerance is not so sensitive to the convergence of adaptive algorithm in our simulations. However, it can affect the density of elements at the interface, thus one can control the minimal element size near the interface by adjusting the tolerance to a certain value.

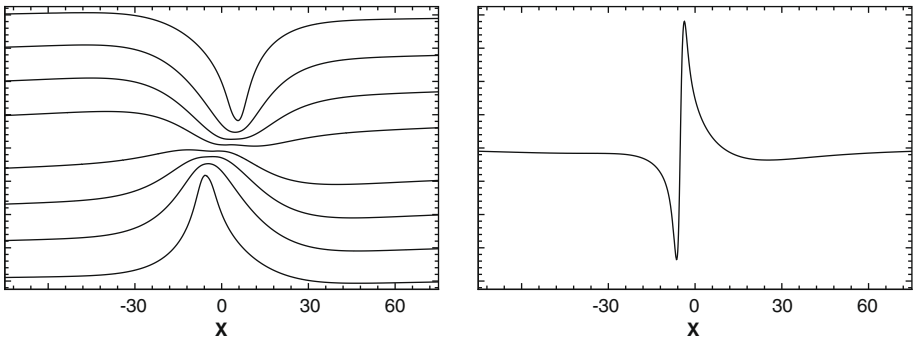

Fig. 1. Couette flow: u_τ profiles at different y planes (left) and pressure variation (right), note the fast variation across the interface.

4. Numerical results

4.1. Comparison with MD simulation

We first validate our multi-mesh algorithm by reproducing the results obtained in [12]. The two immiscible fluids are confined between two parallel walls separated along the y-direction. Moving the top and bottom walls at a constant speed V in the $\pm x$-directions, respectively, induces the Couette flow. We consider the symmetric case in our simulations. That refers to identical wall–fluid interactions for the two fluids, which leads to a static interface with a 90° contact angle. We measured the slip velocity relative to the moving wall u_τ. Our algorithm quantitatively reproduces the interface and velocity profiles from the results in [12], especially the near-complete slip of the contact line and the fast pressure variation (Fig. 1). The components of the solution, velocity parallel to the wall and phase variable, show a very different local behavior, see Fig. 2. The phase field ϕ is constant outside of the narrow interface band, where the phase transition occurs. In order to track the interface, the mesh for ϕ must be refined in the interface band while outside the interface band the mesh can be rather coarse (also see Fig. 7). The velocity u is very smooth except that the gradient changes rapidly around the interface. So to resolve

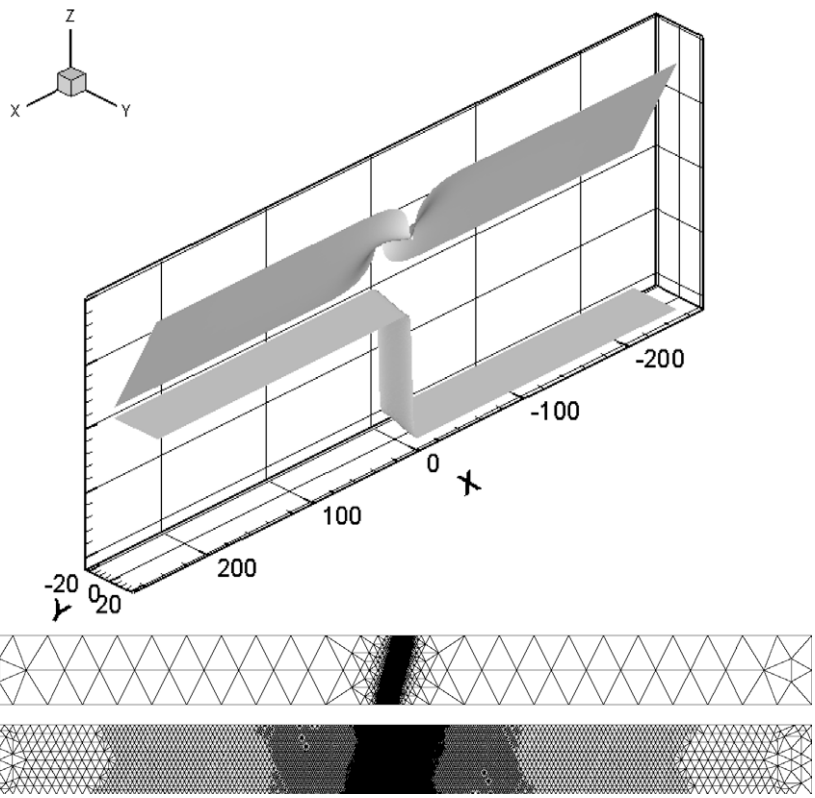

Fig. 2. Couette flow: profile of velocity and phase field (top); adaptive mesh for phase field ϕ (middle); adaptive mesh for velocity **u** (bottom).

its behavior, a much coarser mesh is needed in the interface band than that for ϕ. On the other hand, for accurate solution of the velocity field, the mesh needs to be sufficiently fine enough in the rest of the domain (also see Fig. 6).

4.2. Precursor simulations in spreading

Numerical results have been obtained for the spreading of wetting phase over a rectangle two-dimensional domain of size $L_x \times L_y = 1024 \times 128$. We use the initial condition

$$\phi(\mathbf{x}, 0) = \tanh\left(\frac{R_0 - |\mathbf{x} - (0.5L_x, 0)|}{\sqrt{2}}\right), \tag{4.1}$$

which represents a half-circle shaped fluid–fluid interface with $\mathbf{x}_0 = (0.5L_x, 0)$ as the center and R_0 as the radius. Here the wetting phase (of $\phi = 1$) is initially put in a half-circle region $\{|\mathbf{x} - \mathbf{x}_0| \leqslant R_0\}$. Because of symmetry, only the right part of the whole domain, $[0, 0.5L_x] \times [0, L_y]$, is considered. The equations are discretised on two different adaptive meshes as described in last section. The step of time-integration is taken to be $\Delta t = 1.0 \times 10^{-2}$.

4.2.1. Precursor film in development

Fig. 3 shows the time evolution of the fluid–fluid interface for $\mathcal{A} = 400$ and $b = 1.5\xi$. The results obtained demonstrate several features that are found in almost all the calculations performed in the regime of complete wetting [4,11]. As soon as the VW interaction is turned on, there is a local, fast deformation of the interface immediately above the real contact line. As the wetting phase is pulled toward the solid, its base has to expand and penetrate into the nonwetting phase. As the VW force takes effect only in a narrow range due to the $(y + b)^{-4}$ dependence, this penetration takes place near the surface, within a distance of a few b's. The near-surface penetration continues further into the nonwetting phase and a precursor film is formed which develops progressively ahead of the nominal contact line, i.e., the macroscopic edge of the spreading droplet.

4.2.2. Transition from partial wetting to complete wetting

The free energy per unit area of a liquid film of thickness h on a flat substrate, includes a contribution from the solid–liquid interfacial tension γ_{SL}, a contribution from the liquid–vapor interfacial tension γ and a contribution due to the long-range molecular interactions, van der Waals interaction,

$$V_{VW}(h) = \int_0^h dy\left[-\frac{A}{6\pi(y+b)^3}\right] = \frac{A}{12\pi(h+b)^2} - \frac{A}{12\pi b^2}, \tag{4.2}$$

which quickly saturates at $V_{VW}(\infty) = -A/12\pi b^2$ for $h \gg b$. The spreading coefficient, which takes into account both the short-range and long-range interactions, is given by

$$S = \gamma_{SV} - [\gamma_{SL} + V_{VW}(\infty)] - \gamma = \gamma\cos\theta_s + \frac{A}{12\pi b^2} - \gamma = \left(\cos\theta_s + \frac{a^2}{2b^2} - 1\right)\gamma. \tag{4.3}$$

The value of $S = 0$ separates the regime of partial wetting and that of complete wetting. A sufficiently strong VW interaction leads to the complete wetting with $S > 0$.

The qualitative difference between the final equilibria reached in the two distinct regimes is in fact reflected in the spreading dynamics. As shown in Fig. 4, there is indeed a transition in the spreading behavior across some critical value

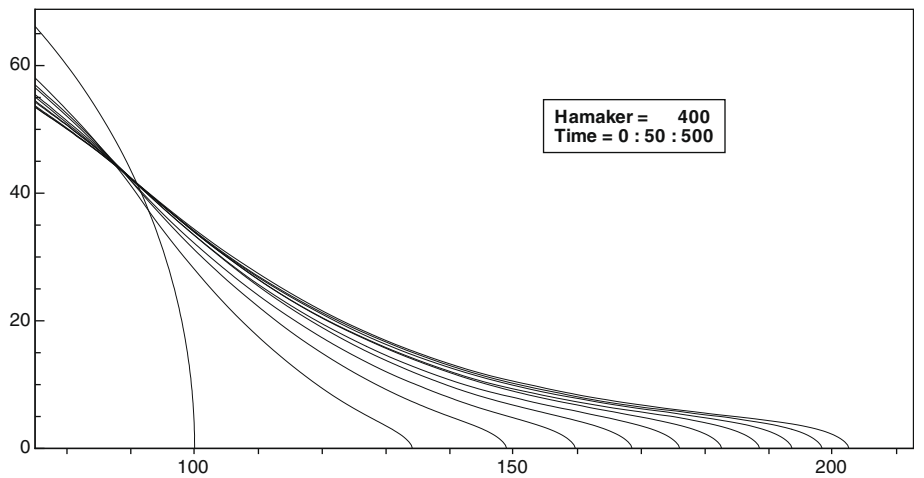

Fig. 3. The time evolution of the fluid–fluid interface calculated for $\mathcal{A} = 400$ and $b = 1.5\xi$. The time interval separating the neighboring curves is $\Delta t = 50$. The development of a precursor film is clearly seen.

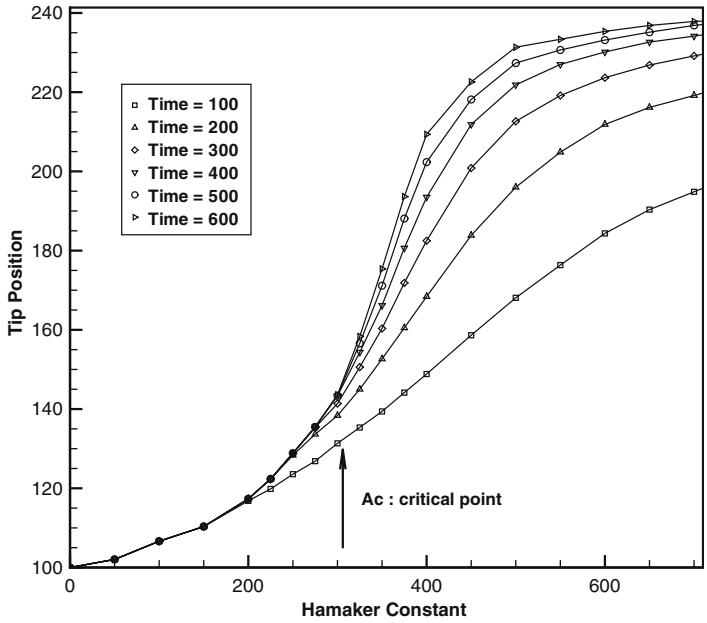

Fig. 4. The distance covered in spreading, plotted as a function of $\mathcal{A}$ for different times *time* = 100 : 100 : 600.

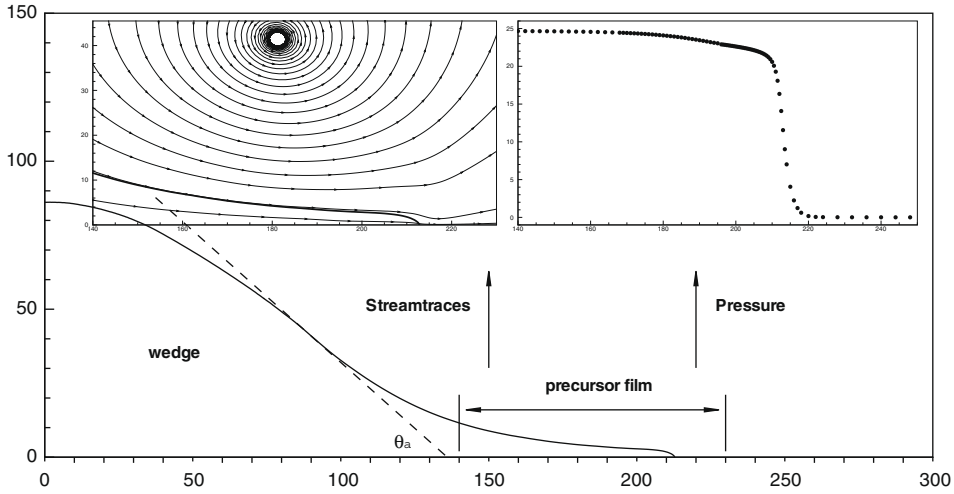

Fig. 5. A precursor film developed ahead of a droplet in spreading, obtained for $\mathcal{A} = 500$ and $b = 1.5\xi$ with $t = 300$. Inset: left one is the streamtraces around the tip area and right one is the distribution of the pressure on the solid–liquid interface.

of $\mathcal{A}$, hereafter denoted by $\mathcal{A}_c$, which corresponds to $S = 0$ within numerical error. The values for $\mathcal{A}_c$ determined in Fig. 4, $\mathcal{A}_c \sim 300$ for $b/\xi = 1.5$, agree with those evaluated from $\mathcal{A} = 4\sqrt{2}\mathcal{B}a^2/\xi^2$ with $a^2/2b^2 = 1$ (which corresponds to $S = 0$ for $\cos\theta_s = 0$ according to (4.3)).

4.2.3. Slipping contact line

As shown in Fig. 5, a thin precursor grows ahead of a wedge of a relatively larger scale. The long, flat part of the film is clearly seen, which is truncated quickly at the real contact line when the thickness becomes comparable to b. The advantage of the present model is that the GNBC has been used to account for the fluid slipping at the solid surface in the vicinity of the MCL. This allows an accurate description of the molecular-scale hydrodynamics in this small region. The inset of Fig. 5 shows the velocity field around the tip of the spreading film, where large slippage is clearly seen.

4.2.4. Multi-meshes

Figs. 6 and 7 show the velocity and phase-field meshes, $\mathcal{T}_\phi$ and $\mathcal{T}_p$ at the time $t = 500$ with a zoom into the interface region. Fig. 8 shows the corresponding degrees of freedoms (DOFs) for phase field ϕ and the velocity $\mathbf{u}$ separately over time.

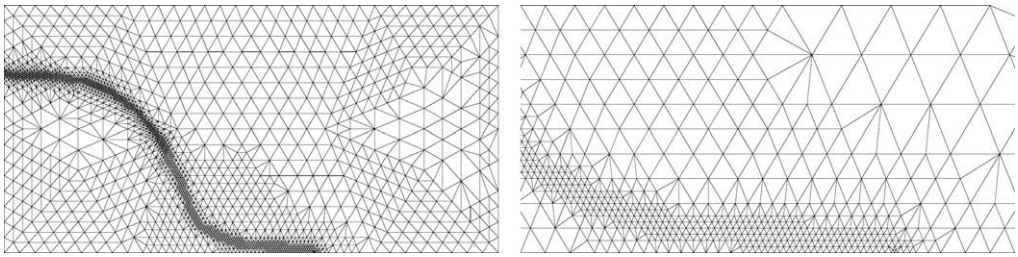

Fig. 6. Velocity mesh (2486 grid points) and zoom to interface at $t = 500$.

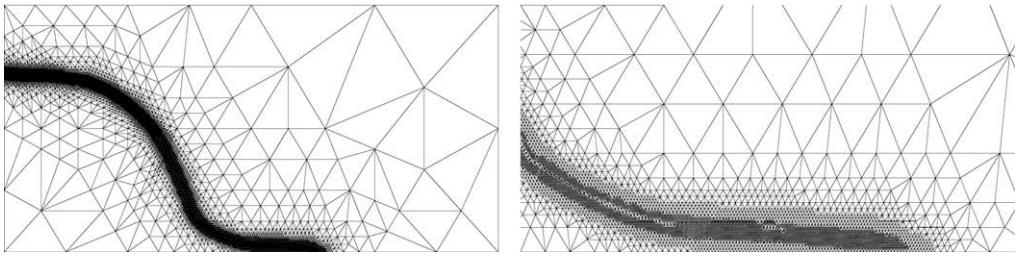

Fig. 7. Phase field mesh (grid points) and zoom at $t = 500$.

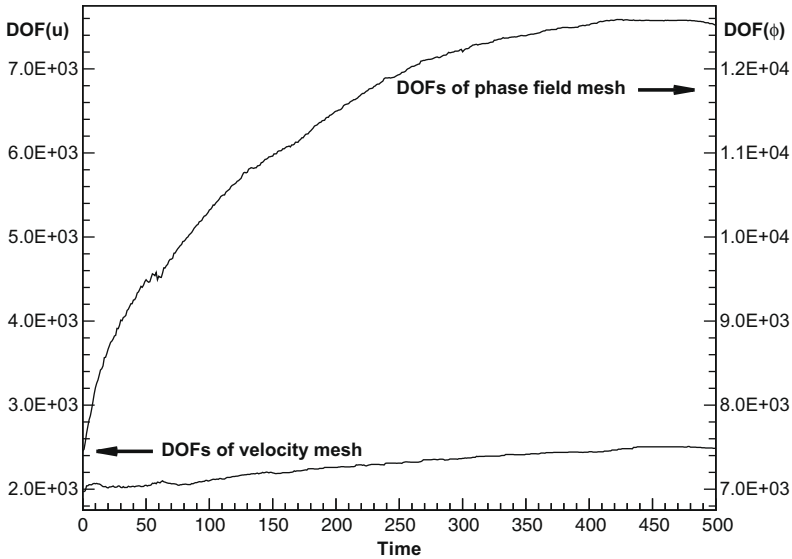

Fig. 8. DOFs over time are shown for ϕ and **u** separately.

The results have shown that the distributions of the meshes for the phase field solution and velocity field solution are very different. Near the interface, finer mesh is needed for the phase field than that for the velocity field. On the other hand, a much coarser mesh is needed away from the interface for the phase field than that for the velocity field. This justifies the use of the two mesh adaptive method.

5. Concluding remarks

In this work, we have developed a multi-mesh adaptive finite element method to investigate the wetting dynamics, focusing on the development of the precursor film and the dissipation therein in the early stage of spreading. We use the diffusive interface model incorporating the long range VW interaction effect together with the recently discovered generalized Navier boundary condition (GNBC) for the simulations. The computational cost can be saved significantly using our multi-mesh adaptive technique. We have studied the early stage of spreading, when the precursor is initiated and developed if the van

der Waals forces are strong enough. We find that there is a transition in the spreading behavior across a critical value of the Hamaker constant which separates the partial wetting from complete wetting.

Acknowledgments

The authors acknowledge helpful discussions with Tiezheng Qian and Ping Sheng. This work was partially supported by the National Science Foundation of China under the Grant 10701075 and the Hong Kong RGC central allocation Grant CA05/06.SC01 and RGC CERG 603107.

References

[1] M. Brezina, Algebraic multigrid based on element interpolation (amge), SIAM J. Sci. Comput. 22 (5) (2000) 1570–1592.
[2] H.Y. Chen, D. Jasnow, J. Viñals, Interface and contact line motion in a two phase fluid under shear flow, Phys. Rev. Lett. 85 (8) (2000) 1686–1689.
[3] A.J. Cleary, Robustness and scalability of algebraic multigrid, SIAM J. Sci. Comput. 21 (5) (1999) 1886–1908.
[4] P.G. de Gennes, Wetting: statics and dynamics, Rev. Mod. Phys. 57 (3) (1985) 827–863.
[5] Y. Di, R. Li, T. Tang, A general moving mesh framework in 3d and its application for simulating the mixture of multi-phase flows, Commun. Comput. Phys. 3 (2008) 582–602.
[6] X. Hu, R. Li, T. Tang, A multi-mesh adaptive finite element approximation to phase field models, Commun. Comput. Phys. 5 (2009) 1012–1029.
[7] D. Jacqmin, Contact-line dynamics of a diffuse fluid interface, J. Fluid Mech. 402 (January) (2000) 57–88.
[8] H.P. Kavehpour, B. Ovryn, G.H. McKinley, Microscopic and macroscopic structure of the precursor layer in spreading viscous drops, Phys. Rev. Lett. 91 (19) (2003) 196104.
[9] R. Li, On multi-mesh h-adaptive algorithm, J. Sci. Comput. 24 (3) (2005) 321–341.
[10] C. Liu, J. Shen, A phase field model for the mixture of two incompressible fluids and its approximation by a fourier-spectral method, Physica D 179 (2003) 211–228.
[11] L.M. Pismen, Y. Pomeau, Disjoining potential and spreading of thin liquid layers in the diffuse-interface model coupled to hydrodynamics, Phys. Rev. E 62 (2) (2000) 2480–2492.
[12] T. Qian, X.P. Wang, P. Sheng, Molecular scale contact line hydrodynamics of immiscible flows, Phys. Rev. E 68 (1) (2003) 016306.
[13] T. Qian, X.P. Wang, P. Sheng, A variational approach to moving contact line hydrodynamics, J. Fluid Mech. 564 (2006) 333–360.
[14] R. Rannachor, *h*-Refine strategy: fix threshold method, J. Sci. Comput. 20 (1998) 320.
[15] P. Sepercher, Moving contact lines in the Cahn–Hilliard theory, Int. J. Eng. Sci. 34 (1996) 977–992.
[16] R. Verfürth, A Review of A Posteriori Error Estimation and Adaptive Mesh-Refinement Techniques, Wiley-Teubner, 1996.
[17] H. Wang, R. Li, Mesh sensitivity for numerical solutions of phase-field equations using *r*-adaptive finite element methods, Commun. Comput. Phys. 3 (2008) 357–375.
[18] O.C. Zienkiewicz, J.Z. Zhu, A simple error estimator and adaptive procedure for practical engineering analysis, Int. J. Numer. Meth. Eng. 24 (1987) 337–357.